

A laboratory-based tender X-ray monochromator for X-ray absorption fine structure measurements*

Haisheng Yu,¹ Jianqiu Zhu,^{1,2} Jiaying Wu,¹ Yaotian Guo,¹ Song Li,¹
Yan Zhang,¹ Xiaoxu Qian,¹ Jian-Qiang Wang,^{1,2} and Linjuan Zhang^{1,2,†}

¹Key Laboratory of Interfacial Physics and Technology, Shanghai Institute of Applied Physics,
Chinese Academy of Sciences, Shanghai 201800, China.

²University of Chinese Academy of Sciences, Beijing 100049, China.

This paper describes the design and performance of a laboratory-based tender X-ray monochromator for X-ray absorption spectroscopy. The system enables effective absorption spectra measurement within the 2.0-9.0 keV range using Rowland circle geometry: it covers the K edge of 3d transition metals, the L edge of lanthanides and the M edge of actinides. The spectrometer is configured with a 500 mm diameter Rowland circle and integrates a 250 W liquid metal-jet X-ray source, a spherical bent crystal analyzer, and an energy-resolving silicon drift detector. The X-ray source is installed outside the vacuum chamber and remains fixed, while the analyzer crystals and detector are adjusted to change the Bragg angle while maintaining the Rowland condition. The energy resolution is 0.36 - 1.30 eV at 2.0 - 9.0 keV, and the monochromatic flux is approximately 5×10^5 counts/s at 7040 eV. This paper highlights the main characteristics of the spectrometer and demonstrates its capabilities through selected experimental examples. The successful development of this spectrometer especially facilitates research on actinide elements, which are often constrained in synchrotron radiation experiments due to their radioactivity, thus fostering advancements in related nuclear energy fields.

Keywords: Laboratory X-ray spectroscopy, XANES, EXAFS, Tender X-ray

I. INTRODUCTION

X-ray Absorption Fine Structure (XAFS) Spectroscopy can acquire local structural information, making it widely used in science research [1, 2], life sciences [3], environmental studies [4–7], and more. The advent of synchrotron radiation in the 1970s significantly advanced the development of XAFS technology, allowing it to evolve into a distinct experimental technique integrated with synchrotron facilities. [8, 9] However, the application process of synchrotron beam, which are critical to understanding the chemistry and local structure of new materials, faces challenges due to their time-consuming nature. At the same time, the equipment and transportation of radioactive samples for synchrotron radiation in situ XAFS experiments are very complicated. Therefore, there is an urgent need to develop X-ray absorption spectrometers based on laboratory scenarios to be compatible and complementary to XAFS experimental conditions.

X-ray energies and instruments can be divided into soft, tender, and hard X-ray ranges [10, 11]. Currently, most laboratory spectrometers are hard X-ray absorption spectrometers. These spectrometers require crystal monochromators and operate with samples in the air, so absorption is attenuated. However, the absorption and scattering of X-ray by air decreases significantly as the energy of the X-rays increases.

For example, in the actinide field, although the M-absorption edge (3.3-4 keV) of the actinide element has a smaller energy broadening than the L-absorption edge, making it more sensitive to the valence state [12], the X-ray absorption of air in this energy range is significant, and a satisfactory XAFS map cannot be obtained. This range requires a fully in-vacuum, focusing crystal spectrometer.

Commonly used XAFS spectrometers based on laboratory X-ray sources have either dispersive or scanning geometry. The spectrometer geometry and the diffraction characteristics of the analyzer crystal have an impact on the choice and capture of photon energies. X-ray detection is performed simultaneously across a spectrum of energies using dispersive spectrometers employing the Von Hamos design. Different energies of X-rays undergo diffraction at distinct locations on the surface of the crystal analyzer. The X-rays that have undergone diffraction are directed towards a detector capable of spatially differentiating between X-rays with different energy levels. Scanning instruments utilizing Rowland circle geometry offer an improved signal-to-noise ratio but necessitate a more intricate mechanical design [13]. To maintain the Rowland condition, both the analyzer crystals and detector are adjusted to change the Bragg angle. Silicon or germanium is commonly used as materials for the analyzer crystals, with multiple crystal reflections required to cover absorption edges relevant to various elements within the range of X-ray wavelengths. Prior to this work, numerous theoretical calculations on energy resolution were conducted [14]. Therefore, this paper focuses on the introduction and application of a tender energy spectrometer.

This paper introduces the world's first laboratory spectrometer capable of operating in the tender energy range. The instrument is specifically designed to facilitate research on XAFS within the energy range of 2.0-9.0 keV. The spectrometer design is based on Rowland circle geometry, featur-

* Supported by Instrument and Equipment Development Program Chinese Academy of Science (Grant No. YJKYYQ20180066), the National Natural Science Foundation of China (Grant No. 22227809), Shanghai Science and Technology Innovation Action Plan (22142200300), the Science and Technology Talents Program of Shanghai Institute of Applied Physics (SINAP-KJZX-202204) and Strategic Priority Research Program of the Chinese Academy of Sciences (Grant No. XDA 0400000).

Haisheng Yu and Jianqiu Zhu contributed equally to this work.

† Corresponding author, zhanglinjuan@sinap.ac.cn

ing a polychromatic micro-focus X-ray source, a Johann-type spherically bent crystal analyzer, and a silicon drift detector (SDD). The paper continues as follows: In Section II, we outline the spectrometer's design and its setup for conducting XAFS measurements. Section III details the experimental arrangement employed. Section IV introduces the performance of the spectrometer. The subsequent section V, encompasses the presentation and analysis of results, accompanied by considerations that advocate for the extensive utilization and further advancement of laboratory-based approaches. Finally, in Section VI, we provide a concise summary.

II. SPECTROMETER DESIGN

The spectrometer is equipped with a laboratory X-ray source, a bent Johann-type spherical crystal monochromators, an SDD, and a vacuum chamber, all devices controlled by LabVIEW. Fig. 1(a) illustrates a schematic diagram of the main components.

A. X-ray source

Initial X-ray spectroscopy experiments were carried out using hermetically sealed X-ray tubes [15]. The development of more powerful X-ray sources for laboratory data-collection systems necessitates addressing the primary concern of effectively dissipating heat generated by accelerated electrons colliding with the metallic target. Excillum Inc. [16] has developed Metal-Jet X-ray tubes, which are conventional micro-focus tubes that utilize a liquid metal jet instead of a solid-metal anode [15]. The metal-jet supports higher electron beam power, thereby generating higher X-ray flux. Therefore, the D2 from Excillum Inc. was selected for laboratory XAFS measurements. The X-ray source is a high-purity liquid gallium jet anode. The tube has a focal spot size of $20\ \mu\text{m} \times 80\ \mu\text{m}$, which transforms to a point source size of $20\ \mu\text{m} \times 20\ \mu\text{m}$ at a 14.5° take-off angle. The apex angle (opening angle) of the X-ray cone is approximately 8° , covering a circular area of 70 mm diameter on the crystal. The maximum accelerating potential is 70 kV, and the maximum current is 3.57 mA. The X-ray source window is a $50\ \mu\text{m}$ thick beryllium window that transmits 2 keV X-rays only half, and almost all (more than 82%) above 3 keV.

B. Crystal

Johann-type Spherically Bent Crystal Analysers (SBCAs) are used for monochromatizing and focusing polychromatic X-ray "bremsstrahlung" energy. In order to minimize the impact of strain fields resulting from spherical bending on energy resolution, crystal wafers are sliced into strips measuring 15 mm in width prior to being bonded with the glass concave substrate. These strips have energy resolution similar to diced-bent crystals and higher efficiency. All crystals

are purchased from XRS LLC Inc. [17]. The SBCAs possess a bending radius measuring 500 mm and exhibit a surface diameter of 100 mm. To cover as wide a working range as possible within the 2.0–9.0 keV energy range and the spectrometer's angular scanning range (55° – 80°), we are gradually expanding our collection of crystal analyzers. Currently, the available analyzer crystals include: Si (111), Si (220), Si (311), Si (400), Si (331), Si (422), Si (533), Ge (110), and Ge (620). Table 1 provides an overview of the spectrometer crystals currently accessible, including their respective coverage within the first order of reflection across the working range and theoretical energy Darwin width corresponding to those reflections. There is an energy gap between 2.4–3.2 keV due to the fact that Si or Ge do not have crystal planes suitable for the intermediate energy range. Other crystalline materials, such as quartz, can cover this energy range; however, processing quartz spherical crystals is still a challenge.

C. Detector

The spectrometer is equipped with an Amptek Fast SDD for transmission XAFS measurements, effectively capturing the intensity of the diffraction signal throughout the data collection process. The Amptek Fast SDD is a vacuum-compatible detector with excellent energy resolution that suppresses higher-order harmonics in the diffraction signal while minimizing background noise. It features a $500\ \mu\text{m}$ thick silicon sensor layer bonded to the top of the electronic layer, providing an effective area of $50\ \text{mm}^2$. The SDD can achieve a counting rate of up to 1×10^6 counts/s with a peaking time constant of $0.2\ \mu\text{s}$. Its energy resolution is 123 eV at 5.9 keV. Integrated within the SDD is a two-stage Peltier cooling system designed to prevent heat buildup and ensure efficient operation.

TABLE 1. Compilation of crystals currently accessible, along with their respective 2d-spacings, Darwin width corresponding to the energy broadening of different crystal plane.

Crystal	2d (nm)	Energy range (keV)	Darwin width (eV)
Si(111)	0.6271	2.007–2.413	0.23225–0.31464
Si(220)	0.3840	3.278–3.941	0.19729–0.23914
Si(311)	0.3275	3.844–4.621	0.11290–0.13513
Si(400)	0.2716	4.636–5.573	0.12183–0.14527
Si(331)	0.2492	5.052–6.073	0.07556–0.09003
Si(422)	0.2217	5.678–6.826	0.08856–0.10546
Ge(440)	0.2000	6.294–7.567	0.15628–0.18357
Ge(620)	0.1789	7.037–8.461	0.12471–0.14535
Si(533)	0.1656	7.600–9.137	0.03668–0.04367

D. Motors and movement

The X-ray source remains stationary outside the vacuum chamber. The crystal analyzer is mounted on a motorized module that provides vertical and pitch angular adjustments

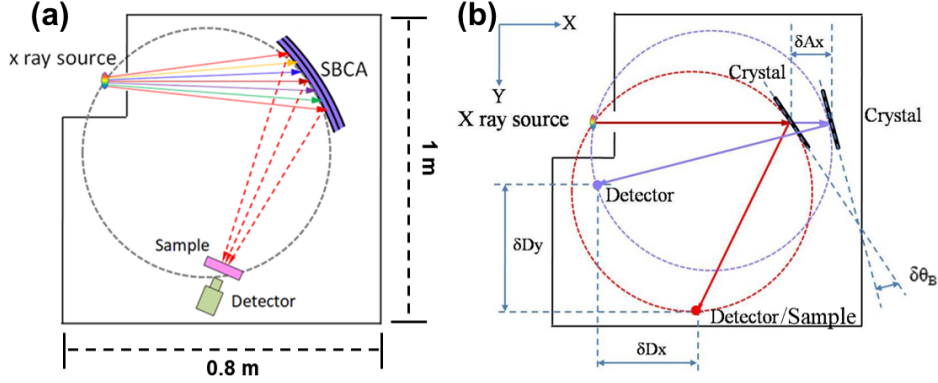


Fig. 1. (a) Design schematic of laboratory X-ray absorption spectrometer based on Rowland circle geometry, (b) Schematic representation of the relative translations (δA_x , δD_x , δD_y , $\delta \theta_{\text{bragg}}$) of motors A_x , D_x , D_y , θ_{bragg} for two different photon energies; the Crystal is maintained on the exact Rowland circle (shown with dotted lines), the center of the coordinate system is the X-ray source.

for alignment, as well as horizontal and rotational adjustments for energy scanning. The goniometer holds the detector, and it is positioned on two linear stages called D_x and D_y in Fig. 1(b). The energy scanning mechanism of the spectrometer follows the Bragg angle equation and trigonometric formulas, which define the geometric requirements for the Rowland circle.

The X-ray source, sample, and bent crystal analyzer are arranged along a Rowland circle with diameter R . With the detector rigidly connected to the sample, which is always directed at the center of the spherical curved crystal by mechanical linkage. For testing, the sample is placed in front of the detector. Whenever there is a change in the Bragg angle θ_B or emitted energy, it becomes necessary to shift the position of the detector along the Rowland circle. Simultaneously, adjustments need to be made to both the angle and distance of the bent crystal analyzer. To maintain optimal focusing geometry, it is essential to keep the detector at an angle Ω that is twice as large as θ_B . When its surface faces towards the X-ray source, this angle Ω becomes zero. Taking the position of the X-ray source serve as the origin of the coordinate system, the X-axis is defined as the direction from the source to the crystal, and the Y-axis is defined as the direction from the source to the detector. Notably, the bent crystal moves exclusively along the X-axis. The spectrometer's motor positions (A_x , D_x and D_y) for a specific photon energy E (measured in eV) are given by:

$$\theta_B = \arcsin \left(\frac{12398.42}{2d_{hkl}E} \right) \quad (1)$$

$$Ax = R \sin \theta_B \quad (2)$$

$$Dx = 2R \sin \theta_B \cos^2 \theta_B \quad (3)$$

$$Dy = 2R \sin^2 \theta_B \cos \theta_B \quad (4)$$

Where R is the radius of the spherical bent crystal analyzer (Rowland circle diameter), θ_B is the Bragg angle, d_{hkl} is the d-spacing for the given crystal orientation/type used, A_x is the x-coordinate of the bent crystal, D_x and D_y the x- and y-coordinates of the detector.

E. Vacuum chamber

The soft X-ray monochromator employs a custom vacuum chamber with a pressure of 10^{-6} mbar, achieved using a 700 L/s vacuum pump. To prevent mechanical deformation from pressure differences, all mechanical components are mounted on a separate sturdy steel plate within the vacuum chamber, ensuring the alignment of the diffraction plane. Due to the volume limitations of individual components, achieving proximity during operation proved challenging, resulting in vacuum chamber dimensions of $1 \text{ m} \times 0.8 \text{ m} \times 0.6 \text{ m}$ and Bragg angles ranging from 55 to 80 degrees.

III. EXPERIMENTAL SETUP

XAFS measurements are conducted in transmission mode. The emission power and spot position of the Metal-Jet X-ray tubes are highly stable, allowing separate measurements of transmitted and direct beams using the same detector. All tests were conducted using the laboratory tender XAFS spectrometer at the Shanghai Institute of Applied Physics, Chinese Academy of Sciences.

In order to demonstrate the capabilities of the instrument, seven samples are shown in Table 2. Due to the presence of spherical aberration, there is a noticeable difference in the focal lengths along the vertical and horizontal directions at the detector side. This discrepancy varies depending on factors such as the Bragg angle and crystal plane. The measurements indicate an approximate range of 4-6 mm for the vertical focal length and 1-2 mm for the horizontal focal length. For XAFS testing in transmission mode, high sample homogeneity

ity is crucial in both laboratory and synchrotron radiation setups [18]. By placing a slit in front of the sample, the spot size can be adjusted accordingly. Additionally, a uniform 10 mm sample can be obtained by pressing, ensuring uniformity over the spot scale.

The test conditions of the samples are shown in Table 2. All metal foils were purchased from Exafs Materials Inc. [19], and TiO₂ was purchased from Aladdin Inc. [20]. The beam intensity was measured without the sample (I_0) and with the sample (I_t), with each scan consisting of 350 energy points, a counting time of 5 s per point, and a motor delay time of 1 s per point. The minimum energy step was set to 0.1 eV. The dead time of all the detectors was less than 25%.

TABLE 2. Summary of sample test conditions.

	Ti	K	U	M ₅	Th	M ₅	Co	K	Ni	K
	edge			edge		edge	edge	edge		
Absorption edge	4966 eV			3552 eV		3332 eV	7709 eV	8333 eV		
Crystal analyzer	Si400			Si220		Si220	Si533	Si444		
Reflection (n)	1			1		1	1	1		
Bragg angle θ_B	66.865			65.367		75.681	76.153	71.626		
samples	rutile TiO ₂	anatase TiO ₂	Ti foil	UO ₂	ThF ₄		Co foil	Ni foil		
Voltage (kV) / Current (mA)	21/ 3.57	21/ 3.57	21/ 3.57	30/ 3.30	30/ 3.30		30/ 3.30	40/ 3.00		
Thickness (μ m)	-	-	6	-	-		4	6		
monochromatic flux with Sample (counts/s)	1.30×10^5	1.30×10^5	1.50×10^5	1.40×10^5	2.10×10^5		2.48×10^5	2.50×10^5		
Energy	0.130	0.130	0.130	0.214	0.200		0.037	0.047		
Darwinian width (eV)	12	12	12	33	6		1	97		

IV. SPECTROMETER PERFORMANCE

A. Monochromatic Flux

The monochromatic flux was tested with Ge (620) crystals in the energy position of 7040 – 7050 eV (Fig. 2(a)). When the voltage was held constant and the current was reduced, the counting rate decreased. The counting rate corresponding to the same power was similar. When the current was held constant and the voltage was increased, the counting rate increased, reaching a maximum at 60 kV, 3.5 mA, and 210 W ($\sim 5 \times 10^5$ counts/s).

B. Energy Resolution

It is difficult to directly evaluate the energy resolution of laboratory source systems; there are two factors contributing to the total energy resolution: the energy broadening corresponding to the core-hole lifetime and the intrinsic energy resolution of the spectrometer. To characterize the spectrometer's energy resolution, we used the characteristic peaks of the X-ray source as a sample to provide a strong signal. The X-ray source operates at 120 W (40 kV, 3 mA) and uses a Si553 crystal monochromator. Fig. 2(b) shows the test results: peaks A and B are fluorescence peaks for gallium K α_2 (9223.8 eV, Bragg angle 71.905°) and K α_1 (9250.6 eV, Bragg angle 71.403°). The full width at half maximum (FWHM) of peaks A and B are 2.96 eV and 2.89 eV, respectively. The energy broadening corresponding to the core-hole lifetime of the Ga K α_2 and K α_1 peaks are 2.66 eV and 2.59 eV, respectively [21]. The final energy resolution of the instrument (ΔE) is 1.298 eV at 9223.8 eV and 1.28 eV at 9250.6 eV.

Additionally, we have theoretically derived the instrument resolution for different energy ranges (Eq. 6). **First, we obtained the ΔE_1 of the crystal based on the tested $\Delta\theta$ and the crystal energy at 71.905°. ΔE_1 is the difference between the energy resolution of the spectrometer and the Energy Darwinian Width of the crystal.** In the laboratory spectrometer system, different energy ranges correspond to different crystal diffraction planes. The Darwin width correction for each diffraction plane is applied to obtain the final instrument resolution (the Darwin width of each crystal at Bragg angle 71.905° is obtained from XAS X-ray data for the elements). As shown in Table 3, the energy resolution ranges from 0.36 to 1.30 eV at 2.0 to 9.0 keV, covering the instrument's energy range.

$$\frac{\Delta E}{E} = \cot \theta \cdot \Delta \theta \quad (5)$$

where the θ is the Bragg angle, ΔE is the Intrinsic energy resolution and the E is the energy.

TABLE 3. resolution for different energy ranges. (The $\Delta\theta$ is 0.00043 rad, the Bragg angle is 71.403° for Si553 at 9250.6 eV and 71.905° for others.)

Crystal	Energy (eV)	ΔE_D	ΔE_1	ΔE
Si553	9223.8	0.02707	1.29572	1.296
	9250.6	0.02715	1.28171	1.282
Si422	5882.9	0.08275	0.82640	0.831
Si331	5234.3	0.07062	0.73529	0.739
Si400	4803.3	0.11389	0.67475	0.684
Si311	3982.7	0.10566	0.55947	0.569
Si220	3396.5	0.18496	0.47712	0.511
Si111	2079.9	0.22680	0.27985	0.360

ΔE_D is Energy Darwin Width, ΔE is Spectrometer Energy Resolution, $\Delta E = \sqrt{\Delta E_1^2 + \Delta E_D^2}$

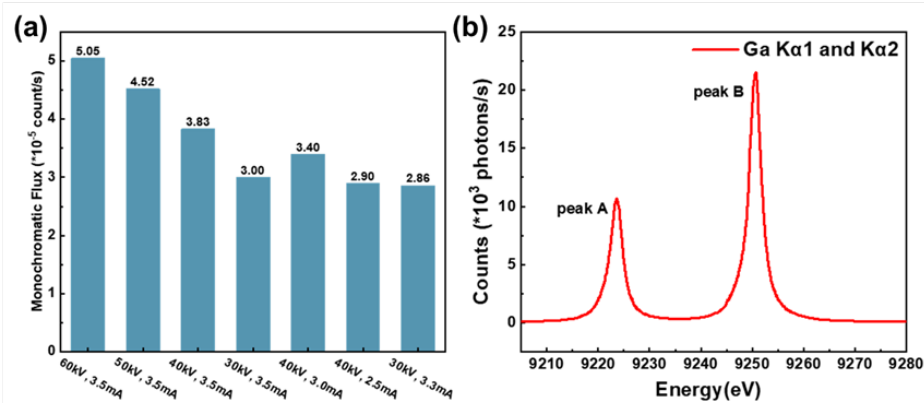


Fig. 2. (a) The monochromatic flux was tested with Ge (620) crystals in the range of 7040-7050 eV in different powder, (b) The fluorescence peaks of gallium $K\alpha_2$ and $K\alpha_1$ were obtained by using the characteristic peaks of the X-ray source.

V. RESULTS AND DISCUSSION

A. XANES

In Figs. 3(a) and 3(b), the normalized K-edge X-ray absorption near edge structure (XANES) of titanium foil and anatase TiO_2 are shown alongside synchrotron data from BL14W1 of the Shanghai Synchrotron Radiation Facility (SSRF). All XAS data were background removed and normalized using the software Athena [22]. The Bragg angle, denoted as $\theta = 66.865^\circ$, was determined based on the first peak observed in the derivative spectrum of Ti foil and assigned a value of 4966 eV. The consistency of the spectra shown in Fig. 3(a) suggests that the energy resolution of the laboratory monochromator is similar to that (1.0 eV) achieved by using a double crystal Si(111) monochromator for synchrotron. Nevertheless, it is crucial to recognize the inherent challenge associated with directly assessing energy resolution in laboratory source systems, encompassing both the measurement of FWHM and comprehensive characterization of the entire energy spectrum. The FWHM of the pre-edge peak of the Ti foil is about 1.2 eV. All features can be reproduced, demonstrating that the lab device is suitable for a wide range of applications.

The XANES spectra of TiO_2 in anatase and rutile forms can be observed in Fig. 3(c). The spectrum consists of pre-edge components A_1 – A_3 , a distinctive shoulder B, and primary peaks C_1 – C_3 . Other reports [26–28] have described the origin of these features. In the rutile TiO_2 sample, features A_1 and A_2 appeared at lower energies compared to the anatase sample, while features B and C appeared at the same energy as in anatase.

In our previous study, we employed a tender X-ray monochromator to analyze MXene materials (a kind of 2D materials [29]), depicted in Fig. 3(d). Our primary focus was on performing near-edge structure analysis of Ti_3AlC_2 and $\text{Ti}_3\text{C}_2\text{Tx}$ materials (a type of MXene), particularly those pertinent to supercapacitor applications [23]. Furthermore, we thoroughly investigated structural attributes and valence changes, building upon these findings.

Unlike the actinide L-edge, the M-edge of actinide elements shows less core energy level broadening and greater sensitivity to the valence states. However, the M-edges of Th (3.3 keV) and U (3.5 keV) are outside the range of hard X-rays (> 5 keV) and have not been effectively tested using laboratory X-ray absorption spectrometers. They are within the energy range suitable for tender X-ray monochromators. The Th and U M-edge absorption spectra were first experimentally examined using a laboratory light source, as depicted in Fig. 3(e) and (f).

Fig. 3(f) shows normalized XANES spectra of UO_2 and $\text{UO}_2(\text{NO}_3)_2$, alongside synchrotron data obtained from beamline XAFCA at the Singapore Synchrotron Light Source (SSLS). The XAFS data were normalized using the software Athena [22]. Compared with XAFCA, SSLS data, the $\text{UO}_2(\text{NO}_3)_2$ and UO_2 spectrum collected by the laboratory spectrometer show a high degree of agreement, indicating that the spectrometer's energy resolution is comparable to that of synchrotron radiation near 3.5 keV. All observed features are reproducible, and this level of replication is adequate for most applications.

In the nuclear energy sector's efforts to immobilize actinide waste efficiently (Fig. 3(g)), we employed conventional U-M4 edge XANES spectra to test the valence state of uranium ions and their coordination environment in U-doped $\text{La}_2\text{Zr}_2\text{O}_7$ -MS samples [24]. In the realm of efficient catalysts (Fig. 3(h)), XANES analysis detected an upward shift in the U-M5 XANES spectra obtained from transmission mode measurements of UCoO_4 catalysts [25], confirming the presence of U^{6+} and providing critical evidence of electronic structure modulation among polymetallic sites.

B. EXAFS

The Bragg angle ranges from 55 to 80 degrees, allowing extended X-ray absorption fine structure (EXAFS) measurements to extend up to or beyond 1000 eV above the absorption edge. Ni and Co foils were selected as samples for different energy ranges. The XAFS data for these samples are

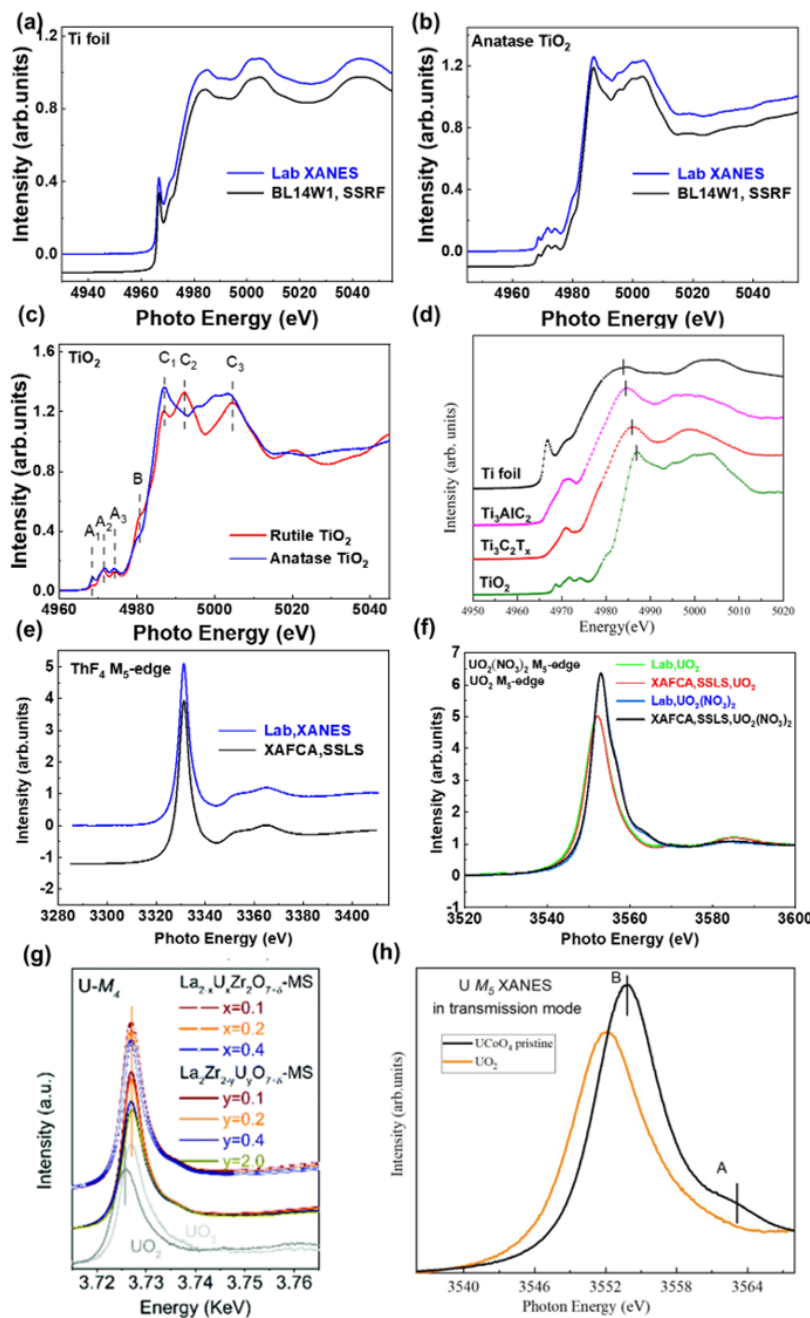


Fig. 3. Normalized K-edge XANES spectrum of (a) titanium foil, (b) anatase TiO₂ compared with synchrotron data obtained at SSRF BL14W1; (c) normalized K-edge XANES spectrum of rutile TiO₂ and anatase TiO₂ based on the laboratory spectrometer; (d) Ti K-edge XANES spectra of the pristine Ti₃AlC₂ before and after MS-etching, together with spectra of Ti foil and TiO₂ references. The Ti K-edge XANES patterns of Ti₃AlC₂ (a type of MXene) before and after MS-etching (Reprinted with permission from Ref. [23]. Copyright 2021 Wiley Online Library). Normalized M₅ edge XANES spectrum of (e) ThF₄ and (f) UO₂ compared with synchrotron data obtained at SSLS XAFCA; (g) U-M₄ edge conventional XANES data of U-doped La_{2-x}Zr_xO_{7-y}-MS samples (Reprinted with permission from Ref. [24]. Copyright 2022 Royal Society of Chemistry); (h) U-M₅ XANES spectra of UCoO₄ (black) and UO₂ (orange) (Reprinted with permission from Ref. [25]. Copyright 2021 ACS Publications).

presented in Fig. 4. Figs. 4c and d show the k-space spectra for the two samples, while Figs. 4e and f display the R-space spectra. The EXAFS spectra obtained from the laboratory spectrometer and Beamline 14W1 at the SSRF are comparable in their k-space oscillations ($2-12 \text{ \AA}^{-1}$), as shown in

Figs. 4 (a-f).

In the realm of electrocatalytic CO₂ reduction (Fig. 4 (g-i)), the transition metal EXAFS of MPc (M=Fe, Co, Ni) catalysts supported on carbon nanotubes were analyzed using the tender X-ray monochromator [30]. The coordination number

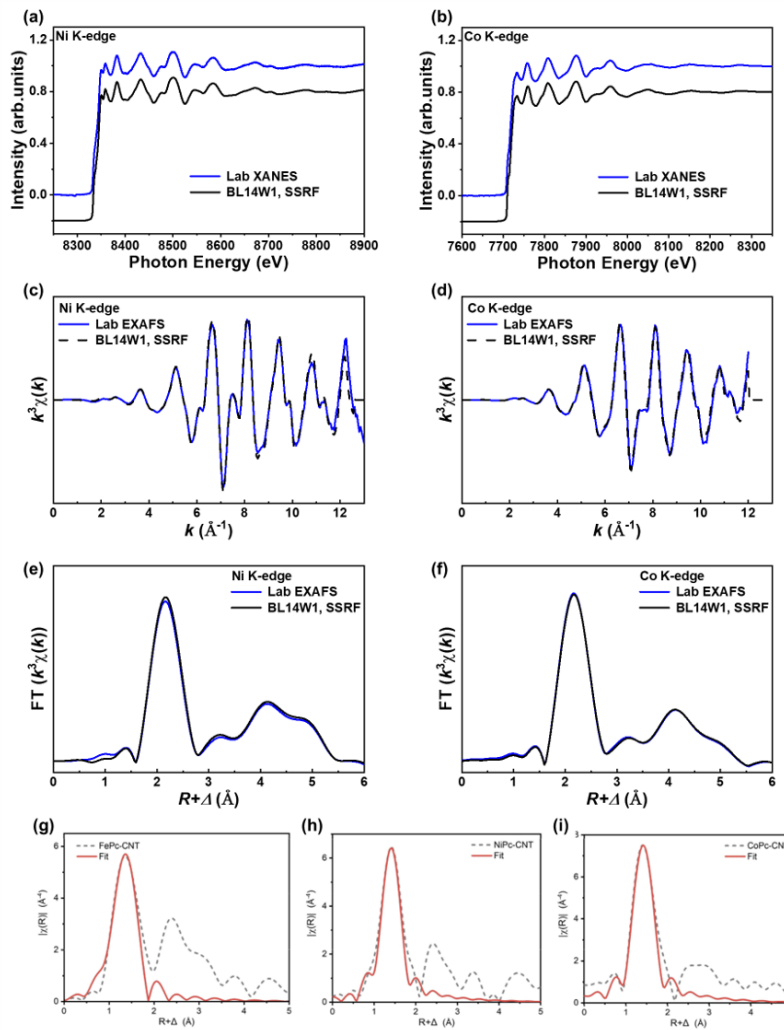


Fig. 4. (a) Ni K-edge XAFS spectrum; (b) Co K-edge XAFS spectrum; (c) Ni K-edge XANES spectrum; (d) Co K-edge EXAFS spectrum; (e) Ni K-edge FT-EXAFS data; (f) Co K-edge FT-EXAFS data; EXAFS spectra of three MPc-CNT samples: (g) FePc-CNT at Fe K-edge; (h) NiPc-CNT at Ni K-edge; and (i) CoPc-CNT at Co K-edge. (Reprinted with permission from Ref. [30]. Copyright 2023 Wiley Online Library)

and bond length were ascertained through the fitting results, significantly contributing to the elucidation of the catalyst's structure.

VI. CONCLUSIONS AND OUTLOOK

We have presented the design and performance of a laboratory-based XAFS spectrometer utilizing an X-ray

source. Laboratory investigations play a crucial role in the preliminary characterization of materials prior to synchrotron analysis. The enhanced configuration incorporates a focusing mirror and positions the sample behind the X-ray source, thereby enabling a broader energy range due to the utilization of high-power X-ray sources and high-count rate detectors. With accessible laboratory spectrometers, XAS has the potential to become a standard method for sample characterization, similar to other X-ray based experimental methods.

[1] D. Koningsberger, B. L. Mojet, J. Miller et al. XAFS spectroscopy in catalysis research: AXAFS and shape resonances. *J. Synchrotron Radiat.* **6**, 135-141 (1999). doi: 10.1107/S0909049599002010.

[2] Z. Liu, Y. Song, X. Xiong et al. Sintering-induced cation displacement in protonic ceramics and way for its suppression. *Nat. Commun.* **14**, 7984 (2023). doi: 10.1038/s41467-023-43725-x.

- [3] R. W. Strange & M. C. Feiters. Biological X-ray absorption spectroscopy (BioXAS): a valuable tool for the study of trace elements in the life sciences. *Curr. opin. struc. biol.* **18**, 609-616 (2008). doi: [10.1016/j.sbi.2008.06.002](https://doi.org/10.1016/j.sbi.2008.06.002).
- [4] J. Zhu, Y. Zhang, Z. Liu et al. Micro-beam XAFS reveals in-situ 3D exsolution of transition metal nanoparticles in accelerating hydrogen separation. *The Innovation Materials*, **2**, 100054-100058 (2024). doi: [10.59717/j.xinnmater.2024.100054](https://doi.org/10.59717/j.xinnmater.2024.100054).
- [5] J. Zhu, J. Cui, Y. Zhang et al. Enhanced H₂ permeation and CO₂ tolerance of self-assembled ceramic-metal-ceramic BZCYb-Ni-CeO₂ hybrid membrane for hydrogen separation. *J. Energy Chem.* **82**, 47-55 (2023). doi: [10.1016/j.jechem.2023.03.027](https://doi.org/10.1016/j.jechem.2023.03.027).
- [6] J. Cui, Y. Zhang, Z. Hu et al. Suppressing Structure Delamination for Enhanced Electrochemical Performance of Solid Oxide Cells. *Small Methods*, **5**, 2300439 (2024). doi: [10.1088/1674-1137/37/2/024102](https://doi.org/10.1088/1674-1137/37/2/024102).
- [7] J. Cui, Y. Zhang, Z. Liu et al. Key Roles of Initial Calcination Temperature in Accelerating the Performance in Proton Ceramic Fuel Cells via Regulating 3D Microstructure and Electronic Structure. *Small Struct.* **5**, 2300439 (2024). doi: [10.1002/ssstr.202300439](https://doi.org/10.1002/ssstr.202300439).
- [8] G. Knapp, H. Chen & T. Klippert. Development of a laboratory EXAFS facility. *Rev. Sci. Instrum.* **49**, 1658-1666 (1978). doi: [10.1063/1.1135340](https://doi.org/10.1063/1.1135340).
- [9] A. Bahgat & K. D. Gupta. A new type of x-ray absorption spectrometer. *Rev. Sci. Instrum.* **50**, 1020-1021 (1979). doi: [10.1063/1.1135970](https://doi.org/10.1063/1.1135970).
- [10] P. Northrup, A. Leri & R. Tappero. Applications of “tender” energy (1-5 keV) X-ray absorption spectroscopy in life sciences. *Protein Pept. Lett.* **23**, 300-308 (2016). doi: [10.2174/0929866523666160107114505](https://doi.org/10.2174/0929866523666160107114505).
- [11] I. Szalóki, J. Osán & R. E. Van Grieken. X-ray spectrometry. *Anal. Chem.* **78**, 4069-4096 (2006). doi: [10.1021/ac060688j](https://doi.org/10.1021/ac060688j).
- [12] C.-O. Almbladh & P. Minnhagen. Comments on core-hole lifetime effects in deep-level spectroscopies. *Phys. Rev. B* **17**, 929 (1978). doi: [10.1103/PhysRevB.17.929](https://doi.org/10.1103/PhysRevB.17.929).
- [13] P. Zimmermann, S. Peredkov, P. M. Abdala et al. Modern X-ray spectroscopy: XAS and XES in the laboratory. *Coordination Chemistry Reviews* **423**, 213466 (2020). doi: [10.1016/j.ccr.2020.213466](https://doi.org/10.1016/j.ccr.2020.213466).
- [14] A.-P. Honkanen, S. Ollikkala, T. Ahopelto et al. Johann-type laboratory-scale x-ray absorption spectrometer with versatile detection modes. *Rev. Sci. Instrum.* **90**, 033107 (2019). doi: [10.1063/1.5084049](https://doi.org/10.1063/1.5084049).
- [15] T. Skarzynski. Collecting data in the home laboratory: evolution of X-ray sources, detectors and working practices. *Acta Crystallogr D: Biol Crystallogr.* **69**, 1283-1288 (2013). doi: [10.1107/S0907444913013619](https://doi.org/10.1107/S0907444913013619).
- [16] Excillum Inc.
- [17] XRS LLC Inc.
- [18] V. R. Mastelaro E. D. Zanotto. X-ray absorption fine structure (XAFS) studies of oxide glasses—a 45-year overview. *Materials* **11**, 204 (2018). doi: [10.3390/ma11020204](https://doi.org/10.3390/ma11020204).
- [19] Exafs Materials Inc.
- [20] Aladdin Inc.
- [21] M. O. Krause & J. Oliver. Natural widths of atomic K and L levels, K X-ray lines and several KLL Auger lines. *J. Phys. Chem. Ref. Data*, **8**, 329 (1979). doi: [10.1063/1.555595](https://doi.org/10.1063/1.555595).
- [22] B. Ravel & M. Newville. ATHENA, ARTEMIS, HEPHAESTUS: data analysis for X-ray absorption spectroscopy using IFEFFIT. *J. Synchrotron Radiat.* **12**, 537-541 (2005). doi: [10.1107/s0909049505012719](https://doi.org/10.1107/s0909049505012719).
- [23] M. Shen, W. Jiang, K. Liang et al. One-pot green process to synthesize MXene with controllable surface terminations using molten salts. *Angew. Chem. Int. Ed.* **133**, 27219-27224 (2021). doi: [10.1002/ange.202110640](https://doi.org/10.1002/ange.202110640).
- [24] J. Sun, J. Zhou, L. Li et al. Atomic controllable anchoring of uranium into zirconate pyrochlore with ultrahigh loading capacity. *Chem. Commun.* **58**, 3469-3472 (2022). doi: [10.1039/D2CC00576J](https://doi.org/10.1039/D2CC00576J).
- [25] X. Lin, Y.-C. Huang, Z. Hu et al. 5f covalency synergistically boosting oxygen evolution of UCoO₄ catalyst. *J. Am. Chem. Soc.* **144**, 416-423 (2021). doi: [10.1021/jacs.1c10311](https://doi.org/10.1021/jacs.1c10311).
- [26] F. Farges, G. E. Brown & J. Rehr. Ti K-edge XANES studies of Ti coordination and disorder in oxide compounds: Comparison between theory and experiment. *Phys. Rev. B*, **56**, 1809 (1997). doi: [10.1103/PhysRevB.56.1809](https://doi.org/10.1103/PhysRevB.56.1809).
- [27] T. C. Rossi, D. Grolimund, M. Nachtegaal et al. X-ray absorption linear dichroism at the Ti K edge of anatase TiO₂ single crystals. *Physical Review B* **100**, 245207 (2019). doi: [10.1103/PhysRevB.100.245207](https://doi.org/10.1103/PhysRevB.100.245207).
- [28] T. Rossi, D. Grolimund, O. Cannelli et al. X-ray absorption linear dichroism at the Ti K-edge of rutile (001) TiO₂ single crystal. *Journal of synchrotron radiation* **27**, 425-435 (2020). doi: [10.1107/S160057752000051X](https://doi.org/10.1107/S160057752000051X).
- [29] K. R. G. Lim, M. Shekhirev, B. C. Wyatt et al. Fundamentals of MXene synthesis. *Nature Synthesis* **1**, 601-614 (2022). doi: [10.1038/s44160-022-00104-6](https://doi.org/10.1038/s44160-022-00104-6).
- [30] Q. Wang, C. Yang, Y. Yan et al. Electrocatalytic CO₂ Upgrading to Triethanolamine by Bromine-Assisted C₂H₄ Oxidation. *Angew. Chem. Int. Ed.* **62**, e202212733 (2023). doi: [10.1002/anie.202212733](https://doi.org/10.1002/anie.202212733).